We are IntechOpen,
the world's leading publisher of Open Access books
Built by scientists, for scientists

6,900
Open access books available

186,000
International authors and editors

200M
Downloads

Our authors are among the

154
Countries delivered to

TOP 1%
most cited scientists

12.2%
Contributors from top 500 universities

CLARIVATE ANALYTICS
BOOK CITATION INDEX
INDEXED

WEB OF SCIENCE™

Selection of our books indexed in the Book Citation Index
in Web of Science™ Core Collection (BKCI)

Interested in publishing with us?
Contact book.department@intechopen.com

Numbers displayed above are based on latest data collected.
For more information visit www.intechopen.com

Mechanical Behavior of Precipitation Hardened Aluminum Alloys Welds

R.R. Ambriz and D. Jaramillo

Additional information is available at the end of the chapter

1. Introduction

Due to its relative low density and high strength, the 2*xxx*, 6*xxx* and 7*xxx* aluminum alloys series are largely used in transportation industry to produce structural frames and compo‐ nents. These alloys find application in artificial aging condition which allows obtaining high mechanical properties, i.e. yield strength of 7075-T651 aluminum alloy as high as 500 MPa. However, when welding processes are used to perform a junction, a large amount of the heat input is dissipated, by heat conduction, throughout the base material close to the welding bead. This thermal dissipation induces localized isothermal sections where the thermal gradient have an important and detrimental effect on the microstructure and therefore on the mechan‐ ical properties of the welded joint (soft zone formation). This microstructural change affects the performance in service of the welded joints, since mechanical properties reduce drastically with respect to base material.

This chapter provides information about mechanical behavior of welded joints of aluminum alloys in terms of properties, determined by tensile, indention and fatigue tests, as well as, the fatigue crack growth conditions in different zones of the welded joints.

1.1. Precipitation and mechanical properties of aluminum alloys

The precipitation hardening process requires that the second component in the aluminum alloy, is sufficiently soluble to allow extensive dissolution at an elevated temperature (solubi‐ lization treatment temperature) and that the solubility is considerably reduced at lower temperatures, such is the case of Al-Cu alloys (Figure 1) [1].

According to Figure 1, to induce precipitation hardening, the alloy is heated at a temperature higher than the solvus temperature to produce a homogeneous solid solution α, allowing

dissolution of the second phase θ and eliminates the segregation of the alloy. Once, the solubilization temperature is reached, the alloy is cooling at high rate in order to limit the diffusion process of the atoms toward potential sites of nucleation. Finally, the supersaturated solid solution α_{ss} is heated at a temperature below the solvus temperature. At this temperature, the atoms have the ability to diffuse at short distances. Because the α_{ss} phase is not stable, the atoms of Cu diffuse at several sites of nucleation and a control precipitation could be formed. Precipitation hardening in metals is performed to produce a particulate dispersion of second phases to generate obstacles for the dislocation movement. The degree of hardening depends of the metallic system, the volume fraction and size of the particles and the interaction of the particles with dislocations. The interactions of the precipitated particles with dislocations are very important in terms of the magnitude of hardening. Some mechanisms have been established, involving particle bypassing by Orowan looping, bypass slip, or particle shearing. Figure 2, shows the forces acting on a mobile dislocation in a stressed metal containing a dispersion of second phase particles.
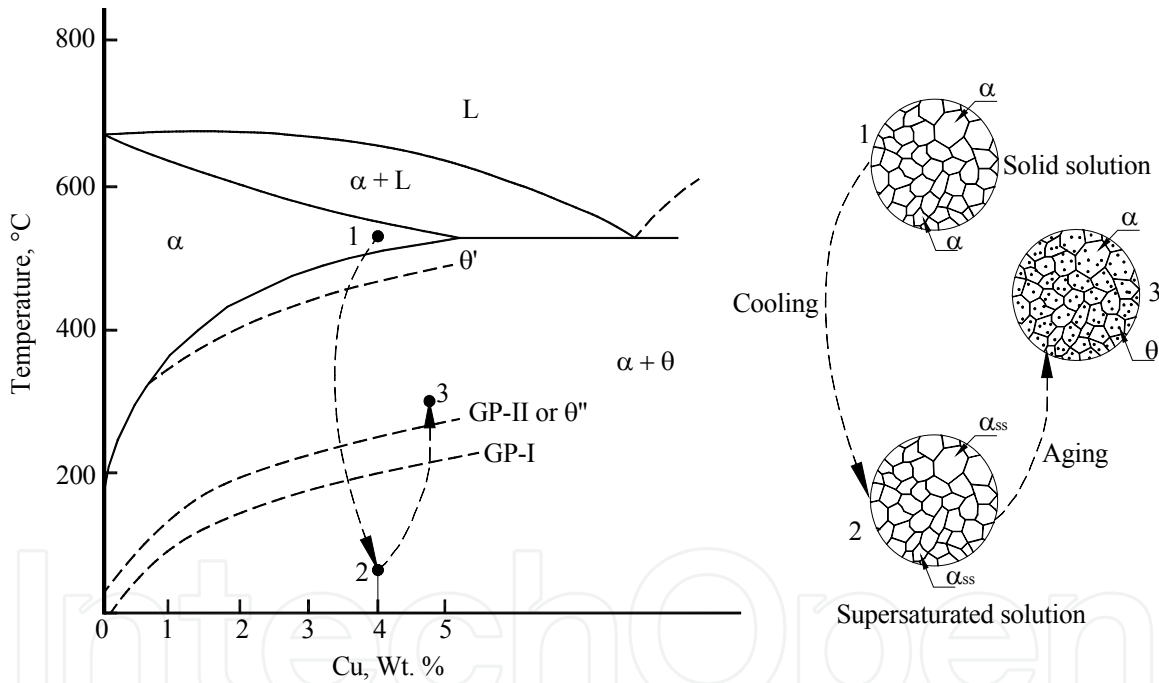

Figure 1. Aluminum-cooper phase diagram rich in aluminum showing the solubilization and precipitation process [1].

Considering the equilibrium forces between the line tension T of the dislocation and the resistance force of the second phase particle F, it is obtained:

$$F = 2T \sin\theta \qquad (1)$$

As F increases, so the bowing of the dislocations increases, i.e. θ increases. The magnitude of F is important in controlling the sequence of events. The dislocation line tension force is
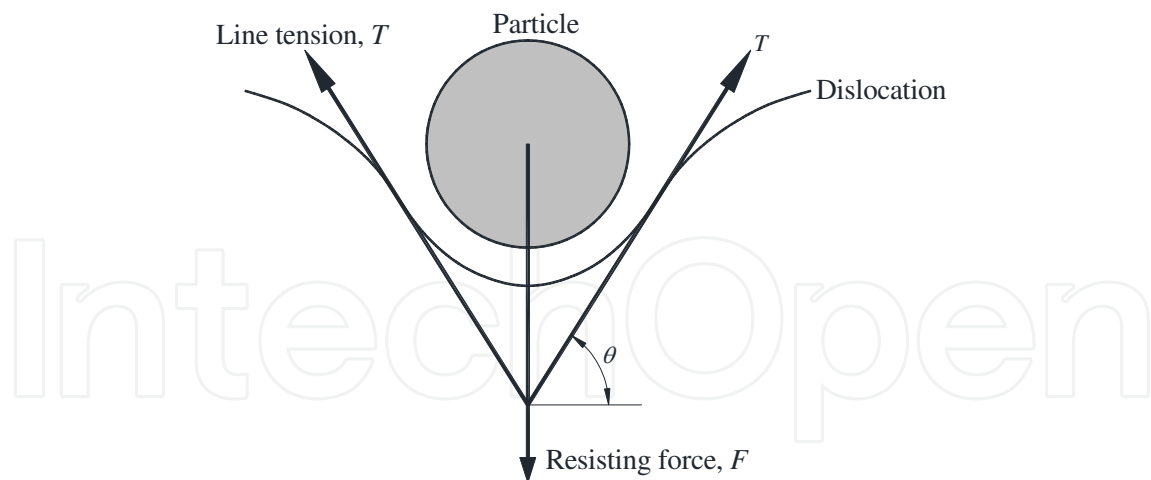
Figure 2. Balance of forces acting during particle resistance to dislocation movement [1].

maximal when θ=90º. If the particle is hard, such that F can be greater than $2T$, then dislocations will bypass the particle either by Orowan looping or cross-slip and the particle will remain unchanged, i.e. non deformed (Figure 3).
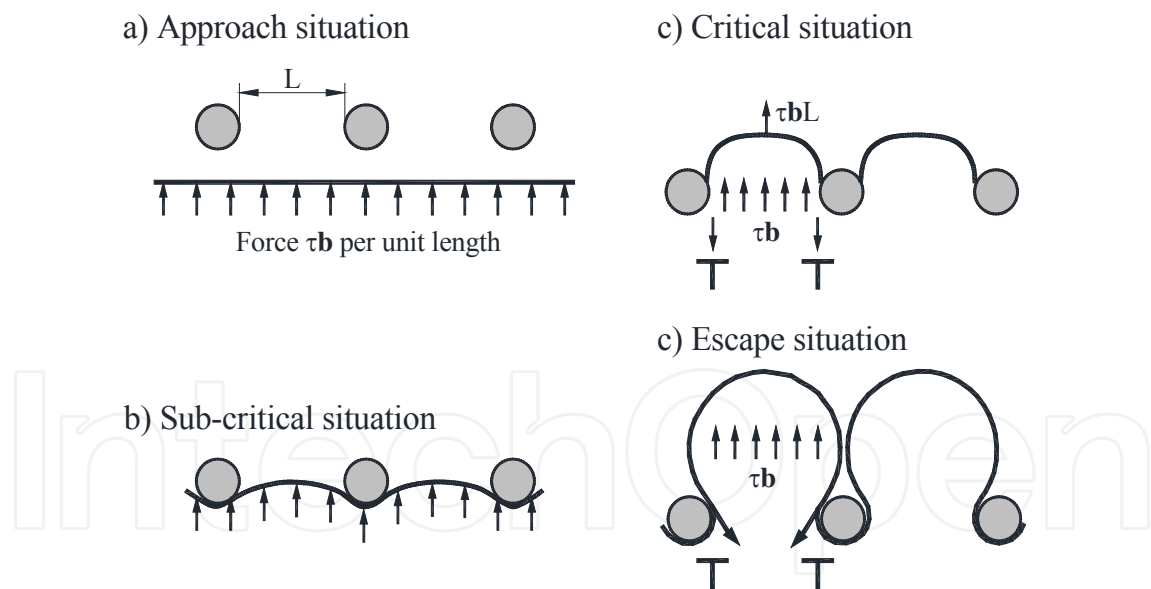

Figure 3. Dislocation meets hard undeformable second phase particles: dislocation release at higher stresses may occur by Orowan looping or by cross-slip [1].

The actual strength of the particle under this circumstance becomes irrelevant, as the bypassing operation becomes dependent only upon the interparticle spacing. If, however, the strength of the particle is such that the maximum resistance force is attained before sin θ=1, then particles will be sheared and the dislocation will pass through the particle (Figure 4).
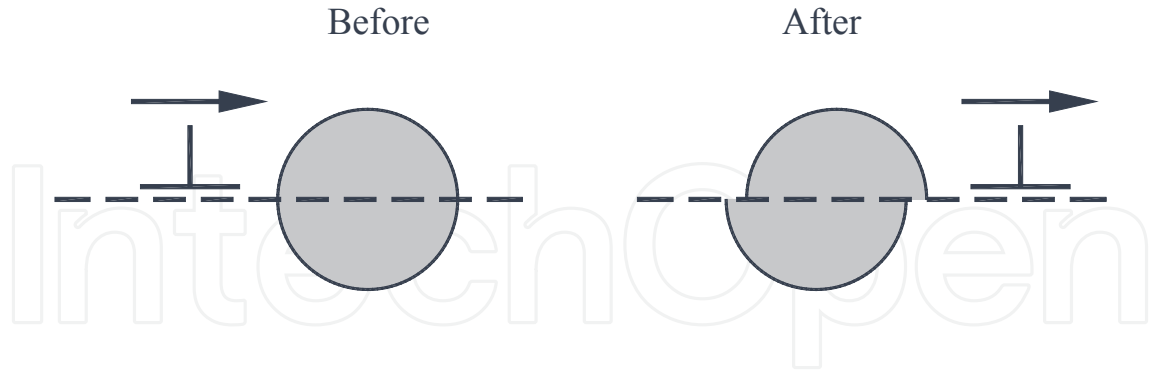
Figure 4. Dislocation motion may continue through second phase particles (particle cutting).

Therefore, it follows that, for a given interparticle spacing (given volume fraction and particle size), hard particles will give the maximum precipitation hardening, and this condition defines the maximum degree of hardening attainable. Soft particles give a lesser degree of hardening. Consideration of the relationship between the applied stress and the dislocation bowing, following Orowan [2], leads to the Orowan equation:

$$\Delta \tau_y = \frac{G\mathbf{b}}{L} \tag{2}$$

where $\Delta \tau_y$ is the increase in yield stress due to the particles, G the shear modulus of the matrix, $\mathbf{b}$ the Burgers vector of the dislocation, and L the particle spacing. The L in the Orowan equation is usually considered to be the distance between particles arranged on a square grid in the slip plane.

Ashby [3] further developed his equation to take into account the interparticle spacing, and the effects of statistically distributed particles. The Ashby-Orowan relationship is given as:

$$\Delta \tau_y = 0.84 \left(\frac{1.2G\mathbf{b}}{2\pi L} \right) \ln\left(\frac{x}{2\mathbf{b}} \right) \tag{3}$$

Application of the Taylor factor for polycrystalline materials, expressing the microstructural parameters in terms of the volume fraction and real diameter and converting shear stress to tensile stress, yields [4]:

$$\Delta \sigma_y = \left(\frac{0.538G\mathbf{b}f^{1/2}}{X} \right) \ln\left(\frac{X}{2\mathbf{b}} \right) \tag{4}$$

where $\Delta\sigma_y$ is the increase in yield strength (MPa), G is the shear modulus (MPa), **b** is the Burgers vector (mm), f is the volume fraction of particles, and X is the real (spatial) diameter of the particles (mm). Table I presents the hardening effect in terms of yield strength for some aluminum alloys in annealed (O) and artificial age hardened conditions (T6).

	Yield strength (MPa)		
Alloy	Annealed condition (O)	Artificial age hardened condition (T6)	Difference
2014	97	417	320
6061	55	276	221
7075	103	503	400

Table 1. Hardening increments in aluminum alloys [5].

1.2. Welding in age hardened condition

The 2*xxx*, 6*xxx* and 7*xxx* aluminum alloys are known to have a strong tendency to overage during welding, especially in fully aged condition (T6). A schematic representation of the microstructural changes in welding of aluminum alloys is shown in Figure 5 [6]. During welding the adjacent metal to the fusion zone (welding bead) is heated and the heat affected zone (HAZ) contents two principal zones. The zone of lower temperature near to the base metal is exposed to a range of temperatures where the aging phenomena and overaging may occur. The zone of higher temperature is treated by solubilization assuming high cooling rate, the effects are less severe, because the microstructure of the material will tend to age in natural manner. However, and isothermal zone appears at within the HAZ for which the obtained temperature is located between two well defined temperatures, i.e. the artificial aging temperature of the alloy and the solvus temperature. As a result a microstructural transformation takes places due to the thermodynamic instability of the precipitates. For instance, in the case of the 6061-T6 alloy, the over-aging in the HAZ is produced by the transformation of the β'' (needle shape) precipitates into β' (rod shape) precipitates according to the following precipitation sequence [7]:

$\alpha_{ss} \rightarrow$ solute clusters $\rightarrow$ GP zones $\rightarrow$ β'' (needle) $\rightarrow$ β' (rod) $\rightarrow$ β

Figure 6, shows the weld thermal cycles for gas metal arc welding (GMAW) process in a 6061-T6 (Al-Si-Mg) alloy at different preheat conditions and their correlation between the C precipitation curve. In this sense, Myhr et al. [9] studied the microstructural evolution during the cooling weld thermal cycle in Al-Si-Mg alloys (Figure 7). They determined that when the peak temperature T_p approaches 315 °C during a period of time of 10 s, the microstructure consists of a mixture of coarse rod-shape β' and fine needle-shape β'' precipitates as shown in Figure 7b and c. The transformation from β'' to β' precipitates occurs to an increasing extent with increasing peak temperatures. At T_p of 390 °C the β' is the dominant microstructural constituent, as indicated in Figure 7d.
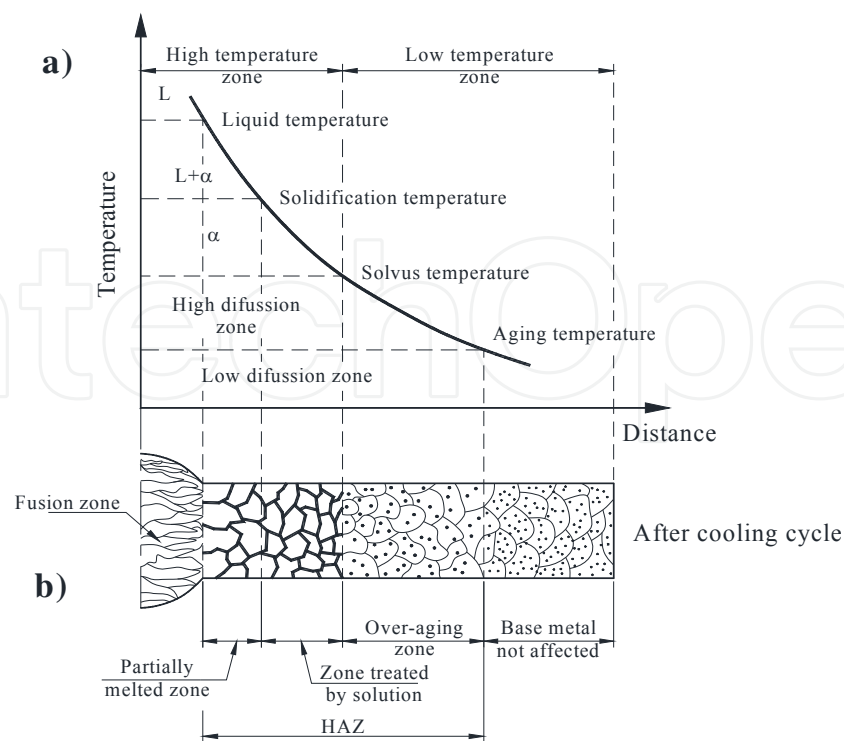
Figure 5. Schematic representation of the microstructural changes in heat treatable aluminum alloys during a fusion welding process, a) cooling thermal cycle from peak temperature, and b) microstructure of the welded joint at ambient temperature [8].
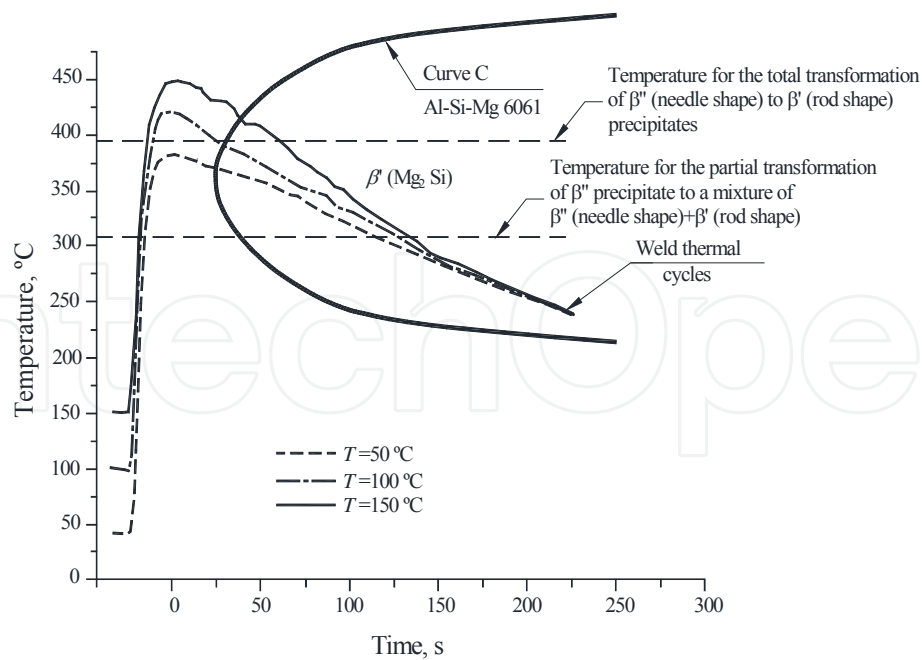

Figure 6. Correlation between weld thermal cycles in gas metal arc welds with three different preheating conditions, and the C precipitation curve for a 6061-T6 aluminum alloy [8].
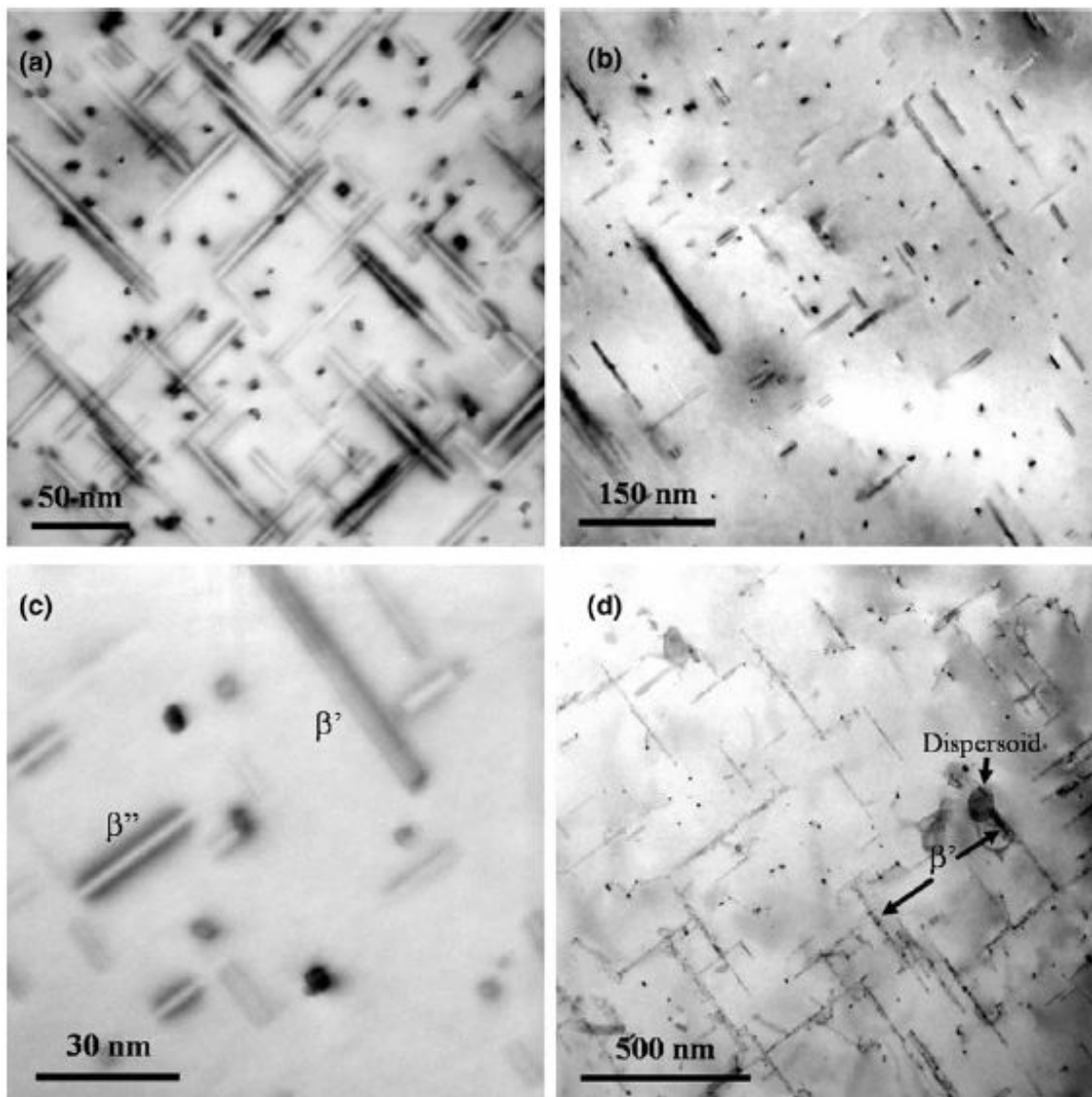
Figure 7. TEM bright field images of microstructures observed in the <100> Al zone axis orientation after artificial aging and Gleeble simulation (Series 1), (a) needle-shaped β'' precipitates which form after artificial aging, (b) mixture of coarse rod-shaped β´particles and fine needle-shaped β´´ precipitates which form after subsequent thermal cycling to T_p=315 °C (10 s holding time), (c) close up of the same precipitates shown in (b) above, and (d) coarse rod-shaped β' particles which form after thermal cycling to T_p=390 °C (10 s holding time) [9].

In addition to the microstructural transformation, after welding porosity and liquation cracking could also exist, which affect directly the mechanical behavior of the welded joints.

Porosity in welds of aluminum alloys is very complicated to control, because of the high hydrogen diffusion in liquid aluminum (Figure 8), the environmental interaction and the high rate of solidification.

When a fusion welding process in aluminum is performed, the hydrogen diffusion in melted metal could be as high as 1.00 cm^3/g, this fact produces the formation of gas bubbles. If we consider the bubble formation in liquid metal as schematically represented in Figure 9, the
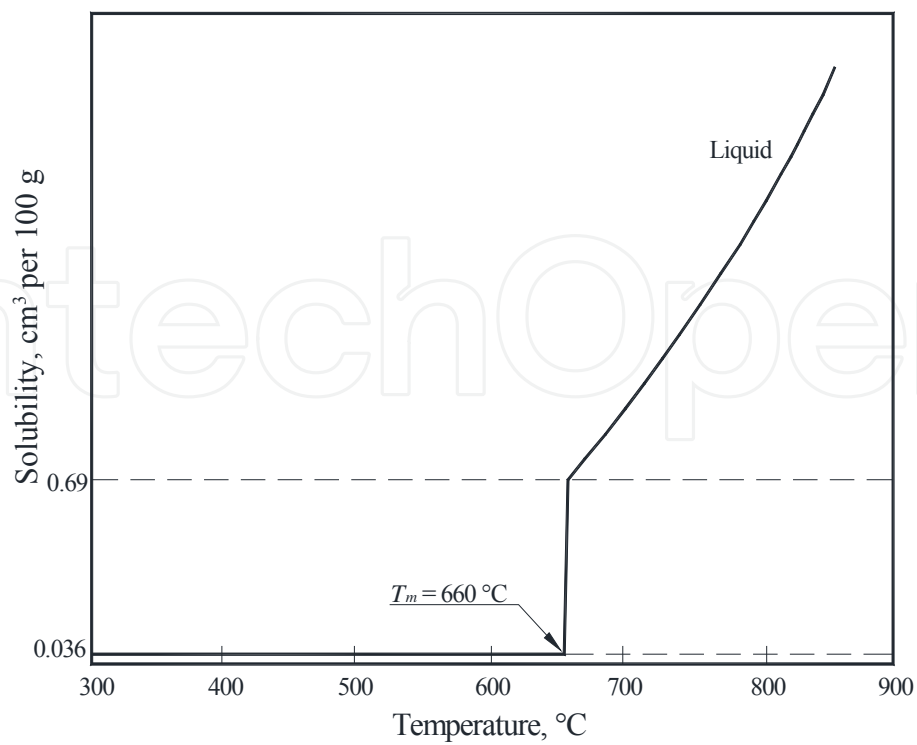
Figure 8. Hydrogen solubility in aluminum [10].

bubble begins to ascend when the surface tension is overcome by the buoyant force, which tends to push the bubble to the free surface.
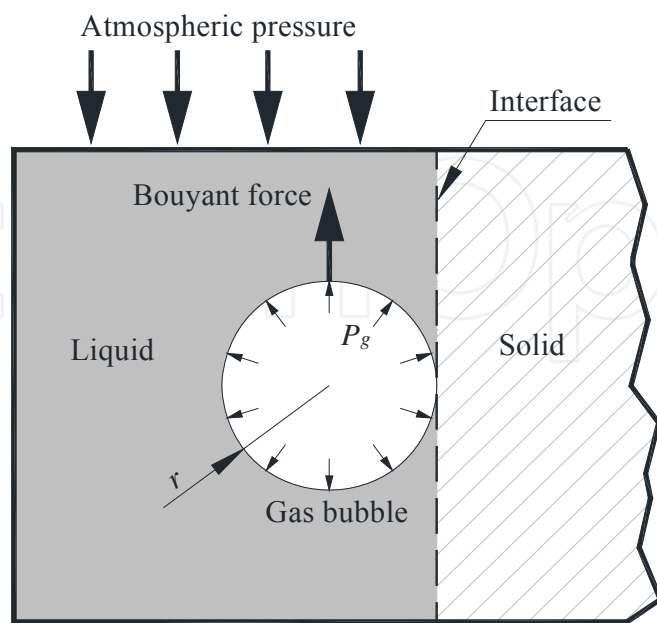

Figure 9. Gas bubble growth due to the diffusion in liquid phase.

The critical radius r_c for the separation of the bubble from the solid-liquid interface can be determined by means of the following expression [11]:

$$r_c = 7.5 \times 10^{-4} \kappa \left[\frac{2\sigma^*}{g(\rho_l - \rho_g)} \right]^{1/2} \qquad (5)$$

where κ is the detaching angle of the bubble, σ^* the interfacial energy between liquid and gas (~ 1 Jm^{-2} for the majority of the gas-metal systems), g the constant gravity force and ρ_l-ρ_g the difference between liquid and gas densities. Considering that densities of liquid aluminum and hydrogen at melting point of aluminum are approximately 2380 kgm^{-3} and 0.0256 kgm^{-3}, respectively, and $\kappa=100°$, the r_c is roughly 700 μm. It is to say that gas bubbles formed during welding process have to be greater than 700 μm to overcome the surface tension of the solid-liquid interface. Additionally, a low solidification rate is needed to allow the gas bubble coalescence and reach this critical value. However, in a real situation the cooling thermal cycle of the fusion zone in welding, is very fast, as demonstrated in [8] (Figure 10), and porosity formation is present as shown in Figure 11.
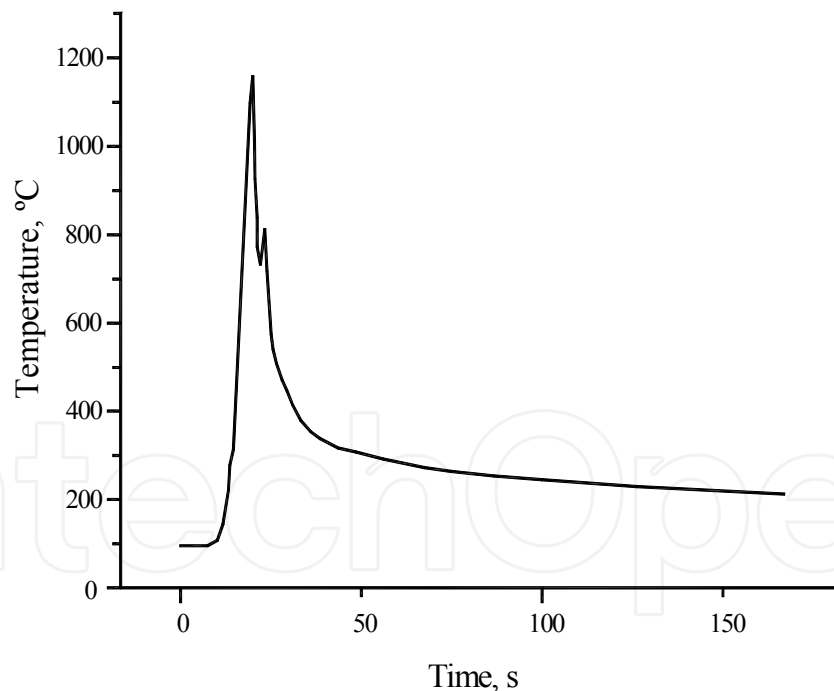

Figure 10. Profile of the temperature measured in the weld pool on a 6061-T6 aluminum alloy GMAW weld [8].

Liquation in welds of aluminum alloys can occur in the partially melted zone (PMZ). The PMZ is the region outside the fusion zone where grain boundary liquation occurs during welding. Figure 12 shows a portion of the PMZ in GMAW of 6061-T6 aluminum made with high silicon content filler metal (ER4043).
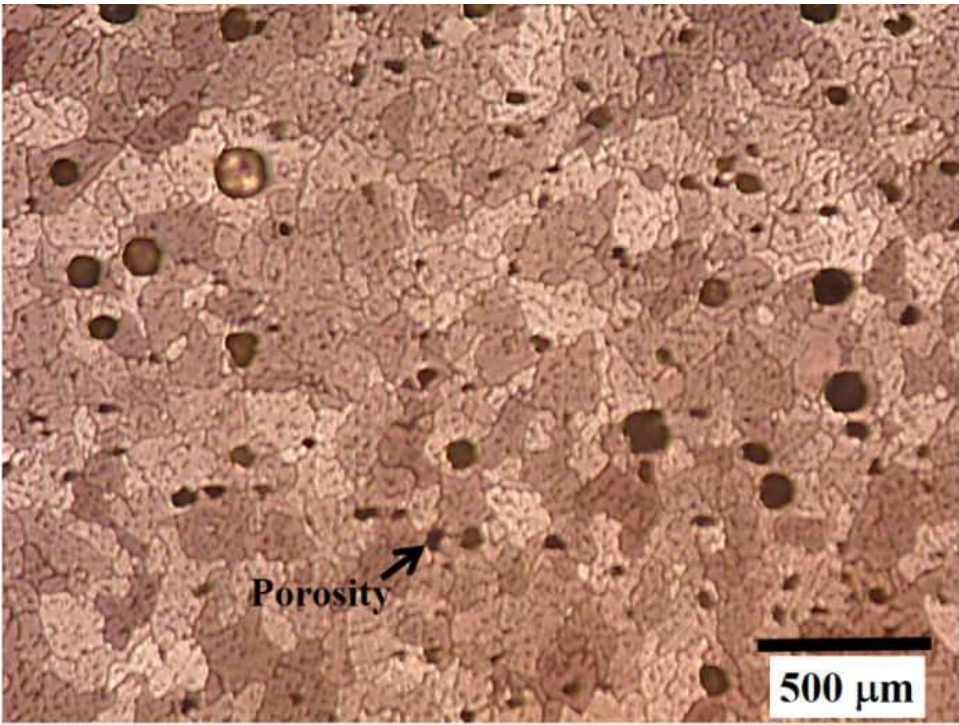
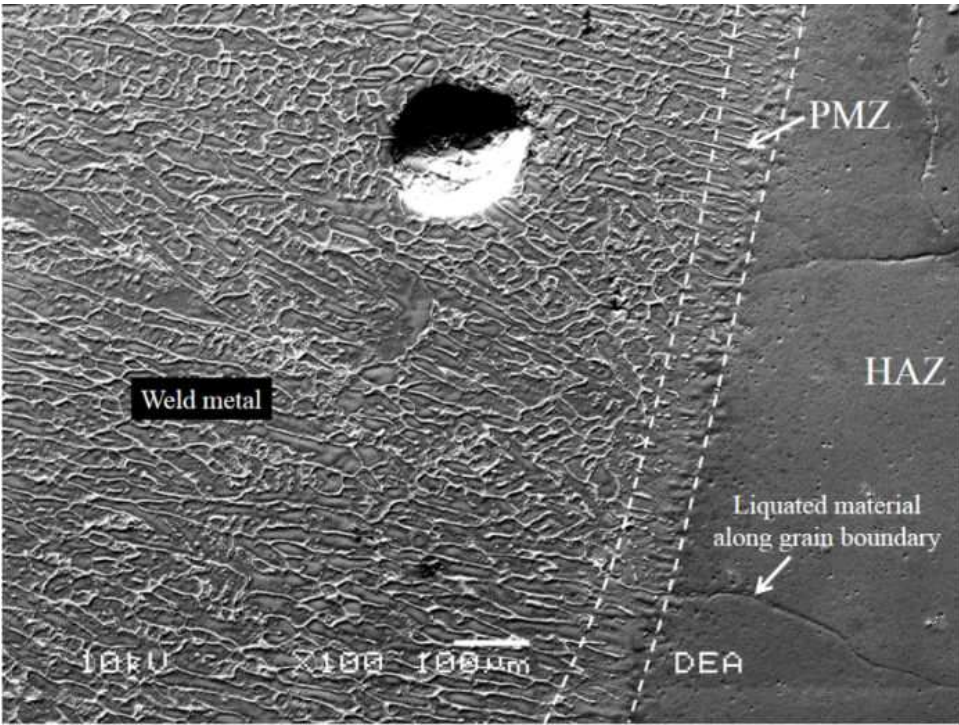**Figure 11.** Weld pool porosity on a 6061-T6 aluminum alloy welded by GMAW.

Figure 12. Microstructure of a 6061-T6 aluminum, welded by GMAW with ER4043 filler metal, showing the PMZ, and grain boundary liquation.

The liquation phenomenon occurs along grain boundary, although it can be presented in the grain interior. When liquation is presented, cracking can occur along grain boundary because of the tensile strains generated during welding. The weld metal composition is determined by base metal and filler metal compositions, as well as, the dilution ratio. The dilution ration is related with the amount of filler metal diluted with the base metal to form the weld metal. Metzger [12] observed liquation cracking in full penetration, gas tungsten arc welding (GTAW) on a 6061 alloy made with Al-Mg filler metal at high dilution ratios, but not in similar welds made with Al-Si filler metals at any dilution ratio. Huang et al. [13] have conducted studies on liquation cracking in the PMZ of full penetration welds of a 6061 alloy. They found that liquation cracking occurred in GMAW welds when an ER5356 (Al-Mg) filler metal is employed but not with an ER4043 (Al-Si).

2. Mechanical behavior of aluminum alloys welds

2.1. Indentation

The hardness of a material represents the plastic deformation resistance by indentation. The hardness number H, is given by the ratio between the applied load P, and a representative area A, of the residual indent:

$$H = \frac{P}{A} \tag{6}$$

For usual indentation, the Vickers hardness number HV, using a pyramidal square based indenter is calculated considering the true contact area. The relation of HV is given by:

$$HV = 1.8544 \frac{P}{d^2} \tag{7}$$

where, sometimes, HV is expressed in MPa if P is given in N and d, the indent diagonal, in mm. But usually HV is given as a number and the conditions of load used.

Concerning instrumented indentation tests (IIT), which allow to plot a load-depth curve, the calculation of a hardness number can use the maximum distance (maximum indentation depth h_m, reached by the indenter during the indentation test) or the contact depth which is the indentation depth h_c, taking into account the deformation of the indent under load and calculated using the method of Olive and Pharr [14].

Classical indentation has been used to determine the hardness evolution in precipitation hardening aluminum alloys welds [8, 15, 16]. Ambriz et al. [8] determined Vickers microhardness profiles and mapping representation in welds of 6061-T6 aluminum alloy (Figure 13).
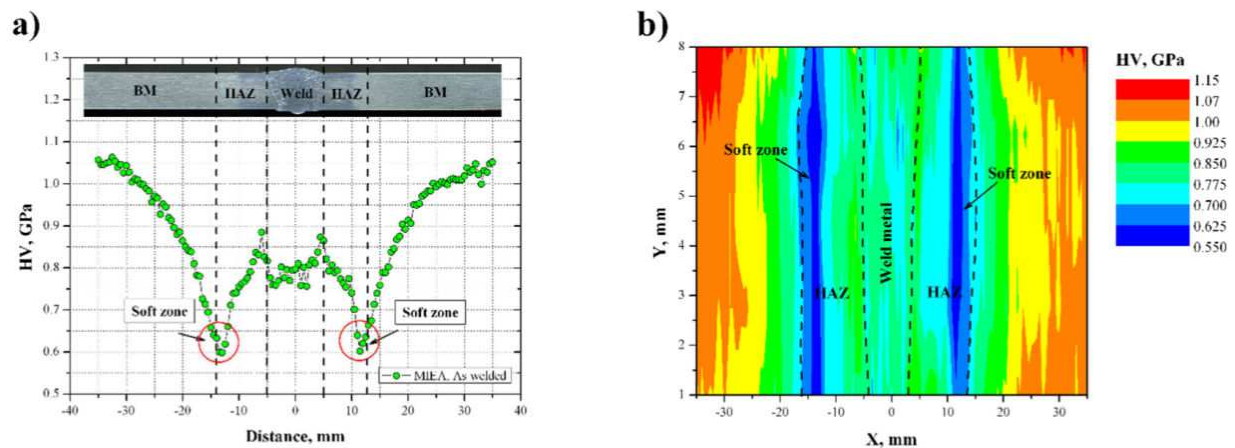
Figure 13. a) Vickers hardness profile determined with 1 N of applied load throughout the welded joint and b) Vickers hardness map over the welded joint [8].

A significant difference for the hardness of weld metal, and HAZ with respect to base material was observed. This indicates that mechanical properties after welding will be different. It should be noted a soft zone formation in both sides of the welded joint, the hardness decrease in the soft zone is around 43% with respect to base material. This characteristic is the result of the thermodynamic instability of the β'' needle-shaped precipitates (hard and fine precipitates) promoted by the high temperatures reached during the welding process. Indeed the temperatures reached during the welding process are favorable to transform the β' phase, rod-shaped according to the transformation diagram for the 6061 alloy (Figure 6).

Considering the hardness heterogeneity of the welded joints, instrumented indentation tests (IIT) was performed in base metal, weld metal and HAZ (soft zone). Figure 14, shows the evolution of the applied load as a function of indentation depth for 6061-T6 and 7075-T651 aluminum alloys welds.
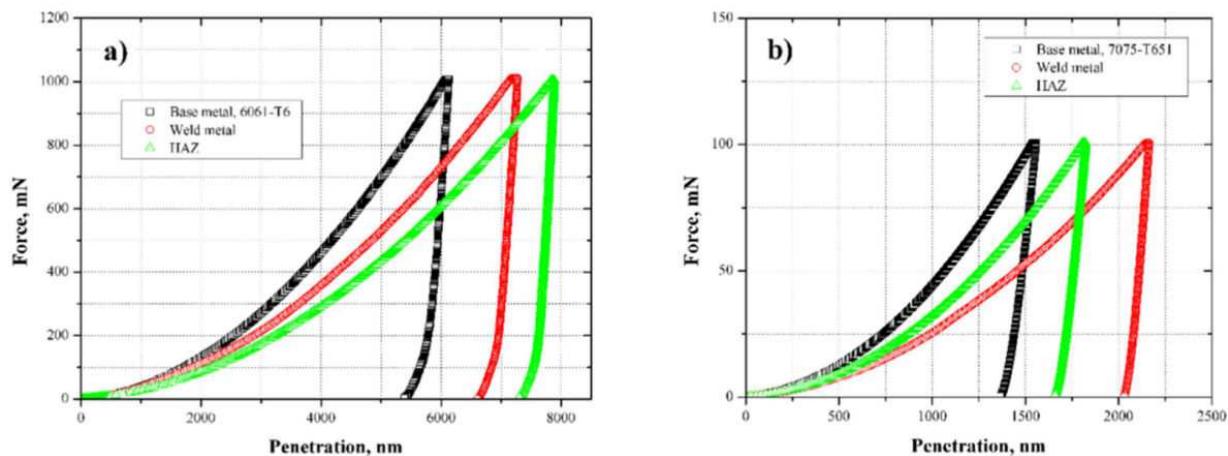

Figure 14. Load-depth curves for a) 6061-T6 aluminum alloy (1 N of applied load) and b) 7075-T651 aluminum alloy (0.1 N of applied load).

Moreover, from the instrumented indentation tests it is possible to calculate the elastic modulus which is deduced by the inverse of the unloading curve (1/S) as a function of the inverse of the contact indentation depth (1/h_c) (equation 6).

$$\left(\frac{dh}{dP}\right) = C_f + \sqrt{\frac{\pi}{24.5}} \cdot \frac{1}{2(\beta \cdot \gamma) \cdot E_R} \cdot \frac{1}{h_c} \tag{8}$$

where $\left(\frac{dh}{dP}\right)$ is the inverse of the contact stiffness, C_f the frame compliance of the indentation instrument, β geometrical factor introduce in the model of Oliver and Pharr [14] to take into account the indenter shape and γ the factor introduced by Hay et al. [17] in the model of Oliver and Pharr for taking into account the approximation in the Hertz's contact analysis and E_R the reduced modulus.

To calculate E_R it is needed to determine a corrective factor due to Hay et al. [17]. This coefficient is only dependent on the Poisson's ratio, then considering a constant value of v_m=0.3 for any region of the welded joint (base material, weld metal and HAZ), it is obtained a value of 1.067 for γ. In this condition, the slope is only linked to the reduced modulus by 0.1653/E_R. Considering 1140 GPa and 0.07 for the elastic modulus and the Poisson's ratio for the indenter material, respectively, it is possible to determine the elastic modulus of the different zones of the welded joints (Table II), by means of the following equation:

$$E_R = \left(\frac{1-v_m^2}{E_m} + \frac{1-v_i^2}{E_i}\right)^{-1} \tag{9}$$

where E_m and v_m are the elastic modulus and Poisson's ratio of the material and E_i and v_i the elastic modulus and Poisson's ratio of the indenter, respectively.

Additionally, the yield strength σ_y and hardening exponent n can be obtained by indentation tests (Table II) as suggested by Ambriz et al. [18], by means of the following expression:

$$P = P_0 + 26.43\sigma_y \left\{\frac{2}{3} + \frac{1}{2}\left(\frac{1}{3}\frac{E}{\sigma_y}\cot(\lambda)\right)^n + \frac{2}{3n}\left[\left(\frac{1}{3}\frac{E}{\sigma_y}\cot(\lambda)^n\right) - 1\right]\right\}h^2 \tag{10}$$

where P is the applied indentation load, P_0 shift indentation load, E elastic modulus, h true indentation depth into material.

Instrumented indentation test allows to determine the properties given in Table II. Yield strength values determined by instrumented indentation are similar to those obtained by micro-traction test (Figure 16). It means that it is possible to characterize a local zone in a welded material by instrumented indentation where it is not possible by global test (tensile test).

Material	E_{IIT} (GPa)	σ_y (MPa)	n	P_0 (N)
Base metal	98.6	266	0.46	0.015
Weld metal	78.0	133	0.48	0.022
HAZ	87.4	106	0.46	0.016

Table 2. Mechanical properties obtained by instrumented indentation test for a 6061-T6 aluminum alloy welds [18].

On the other hand, the elastic modulus obtained by instrumented indentation does not correspond with those reported in tension or compression tests for aluminum alloys (68-72 GPa) and it is not possible to establish a clear difference between weld metal and HAZ. In fact in a recent study, Chicot et al. [19] established that the elastic modulus obtained by instrumented indentation corresponds to a bulk modulus. This was explained by the fact that for the case of indentation, the elastic and plastic strain is triaxial, whereas in tensile test, the strain used to determine the elastic modulus is uniaxial.

2.2. Tensile properties

As possible to deduce from indentation test (Figure 13), the tensile mechanical properties of aluminum alloys welds hardened by precipitation, are not homogeneous along the welded joint. Tensile properties in welds obtained by several welding processes of this alloys have been studied. For instance, V. Malin [15] studied the relation between weld thermal cycles and the microstructural transformation with tensile properties of a 6061-T6 alloy welded by GMAW. In their research, tensile tests samples were taken from the welded joint as shown in Figure 15. It is to say, a global structure effect was considered during tensile test.
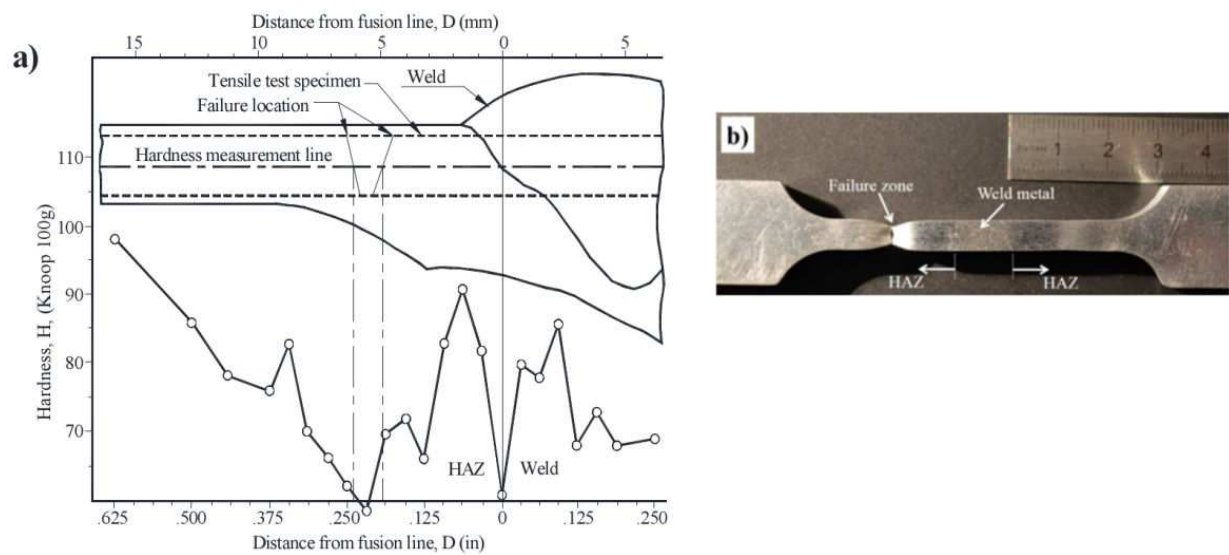

Figure 15. (a) Effect of hardness on HAZ failure location in 6061-T6 tensile specimen [15], and b) tensile sample showing the failure zone on a 6061-T6 aluminum alloy.

The failure zone after tensile test was localized in the HAZ (soft zone) where the hardness of the welded joint is minimal, this result is in agreement with Ambriz et al. [20].

Considering the hardness profile evolution, the true stress-strain curves in weld metal and HAZ (soft zone) of a 6061-T6 alloy welds were determined by means of micro-traction test [18]. The individual behavior is presented in Figure 16, as well as, its respective comparison with base metal.
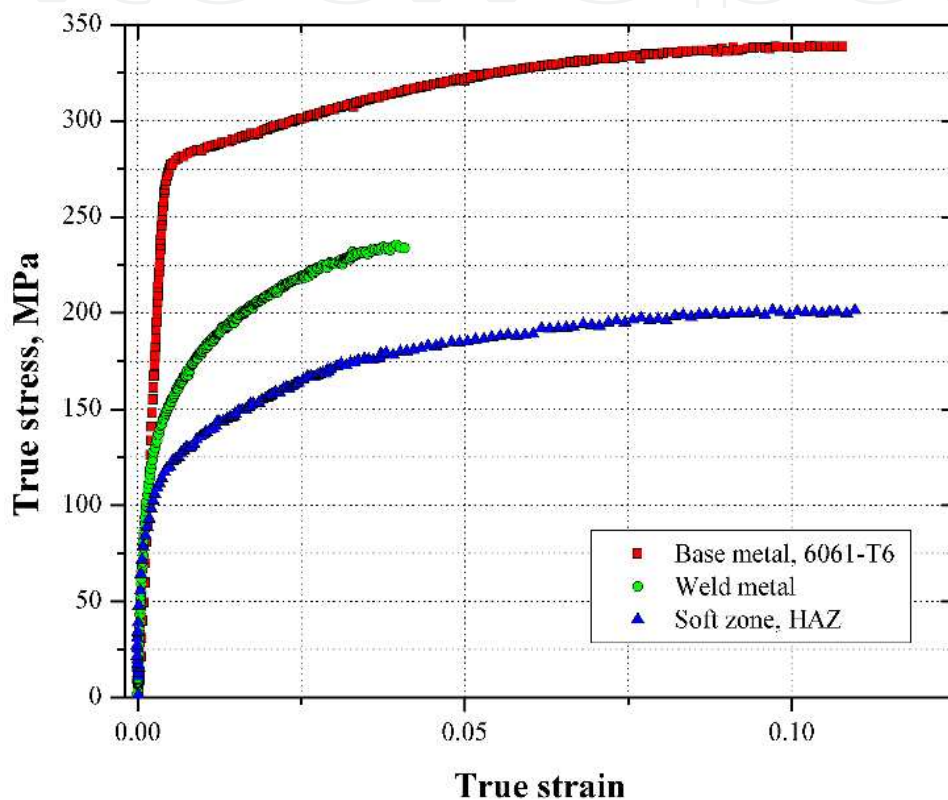

Figure 16. True stress-strain curves for 6061-T6 alloy, weld metal and HAZ.

The HAZ presents a reduction of the tensile strength with respect to base metal and weld metal of around 41 and 19%, respectively. This aspect was related to the over-aging phenomenon and it is explained in terms of the microstructural transformation (Figure 5), and precipitation sequence. Although, weld metal shows higher tensile strength than HAZ, a lower ductility is observed for weld metal. This characteristic was attribute to the porosity formation during the solidification and the high silicon content of the filler metal (ER4043) which, when mixed with the melted base metal, leads to a microstructure of eutectic silicon, which is a brittle phase that adversely affects the tensile mechanical properties of the welded joint. A summary of tensile mechanical properties for 6061-T6 and 7075-T651 aluminum alloys welds are presented in Table III.

Material	E (MPa)[a]	σ_y (MPa)	σ_u (MPa)[b]	ε (%)[c]	H (MPa)[d]	n[d]
6061-T6	68	279	310	14.0	408	0.08
6061-T6 (weld metal, ER4043)	68	151	226	4.00	464	0.20
6061-T6 (HAZ, soft zone)	68	120	183	13.0	300	0.16
7075-T651	72	530	568	8.00	794	0.08
7075-T651 (weld joint, ER5356)	68	165	260	2.80	677	0.25

[a] Best linear fitting from mean stress-strain curves; [b] Obtained from $\sigma = \frac{P}{A_0}$; [c] obtained from $\varepsilon = \frac{l_f - l_0}{l}$, [d] obtained by Ramber-Osgood equation.

Table 3. Tensile mechanical properties of 6061-T6 and 7075-T651 aluminum alloys welds (GMAW).

2.3. Fatigue of aluminum alloys welds

Fatigue or fatigue damage is the consecutive modification of the materials properties with respect to the application of a cyclic stress, which can conduct to the fracture. Under uniaxial cyclic loading conditions it is possible to distinguish a stress ratio R determined by a maximal and minimal stress as follow:

$$R = \frac{\sigma_{\min}}{\sigma_{\max}} \tag{11}$$

As a function of σ_{max} and σ_{min}, we can obtain the constant component of the stress (amplitude stress σ_a) and the mean value of the stress (mean stress σ_m) by different loading conditions (Figure 17).

Some practical applications involve cyclic loading at a constant amplitude, but irregular loads as a function of time are commonly encountered. In this case, we will discuss some results in terms of a constant amplitude loading. The simplest fatigue test consists of subjecting a specimen to a cycling loading (different levels of stress amplitude σ_a), at a constant frequency and measured the number of cycles to failure N_f. The representation of stress level as a function of N_f gives the S-N curve or Wöhler curve. A schematic representation of a Wöhler curve is shown in Figure 18.

In Figure 18, it is possible to identify different domains: (i) Low cycle fatigue. In this case a high stress level is applied on the sample (normally over the yield strength of the material). Because of the high deformation during the test, the number of cycles to failure tends to be lower (10^2 to 10^4). (ii) High cycle fatigue. This is related with an elastic behavior on a macro scale of the sample, i.e. the stress level is not higher than the yield strength of the material. The failure is expected for a large number of cycles, for instance, more than 10^5. In fact the boundary between low and high cycle fatigue is not well defined by a specific number of cycles. The most important difference is that low cyclic fatigue is associated with macro-plastic deformation on
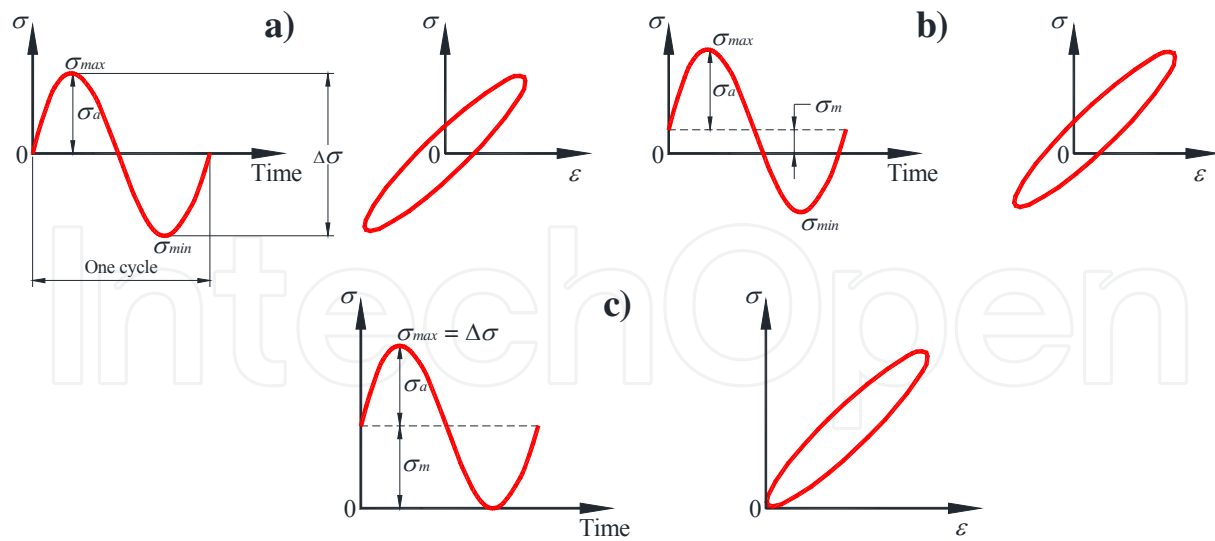
Figure 17. Solicitation loading in uniaxial fatigue, a) completely reversed stressing (σ_m=0), b) asymmetric repeated stressing ($\sigma_m \neq 0$), and c) zero to tension stressing (σ_{min}=0).
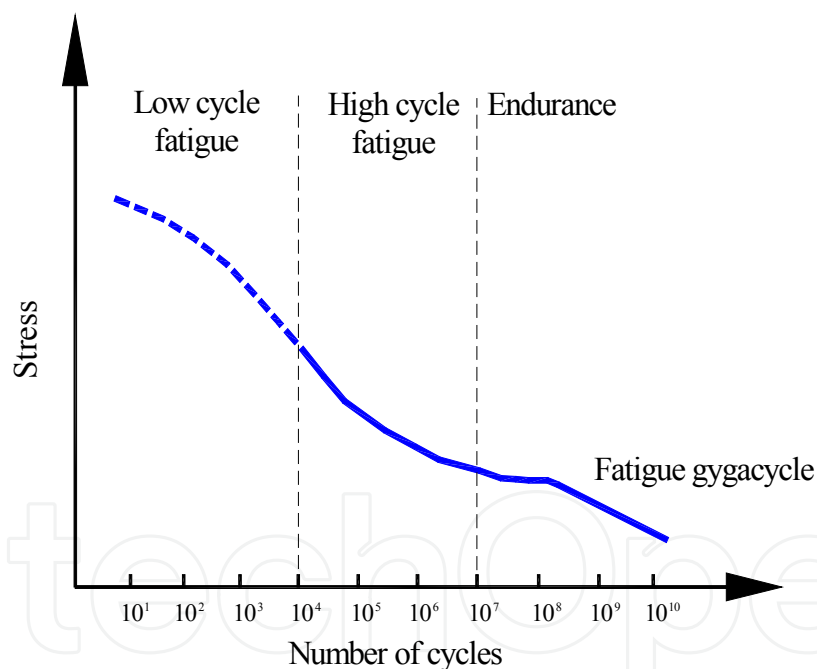

Figure 18. Representation of a Wöhler curve, and different fatigue domains [21].

each loading cycle. When the stress level in high cycle fatigue is applied, a fatigue limit or endurance limited is presented, which is represented by an asymptote in the Wöhler curve. In some metallic materials it could be obtained when the number of cycles is in the order of 10^6 to 10^7. (iii) Fatigue gigacycle. This domain corresponding with a very high number of cycles and it has been observed that fatigue limit tends to decrease when the number of cycles increases.

It is well known that fatigue damage is a surface phenomenon as indicated by Forsyth [22], who determined the presence of reliefs linked to the formation of localization deformation bands named persistent bands. The surface topography is traduced by the formation of intrusions and extrusions as shown schematically in Figure 19.
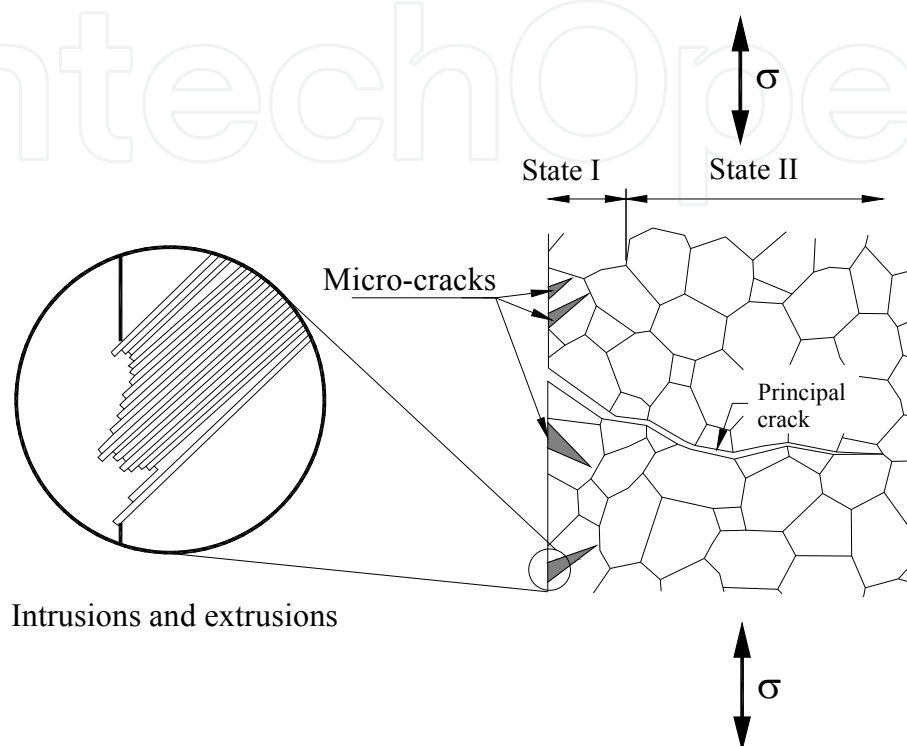

Figure 19. Intrusions and extrusions formation in the free surface due to the alternating slip, micro-cracks nucleation, and principal crack formation from micro-cracks [21].

For a uniaxial tensile test, these bands resulting in the formation of micro-cracks (state I in Figure 19), which are orientated at 45 degrees with respect the traction axe. Only certain grains are affected by the formation of those bands. The persistent bands orientation and the formation of cracks on the state I, are important in the case of uniaxial and multiaxial loading. Brown and Miller [23, 24] introduced a useful notation in multiaxal loading for facets A and B, which are schematized in Figure 20.

The type B facets provides a shearing vector which enters into the material, and they are more dangerous than type A facets, from which the shearing vector is tangent to the free surface of the sample. The intrusions and extrusions formation associated to the slip persistent bands, as well as, the micro-propagation of cracks in the state I are of interest at a distance of the grain size (small fatigue cracks). Thus, considering that micro-cracks are related with the crystallography aspect, once the crack encounters the first grain boundary it begins to bifurcate according to state II and the propagation at a perpendicular direction of the principal stress is obtained.
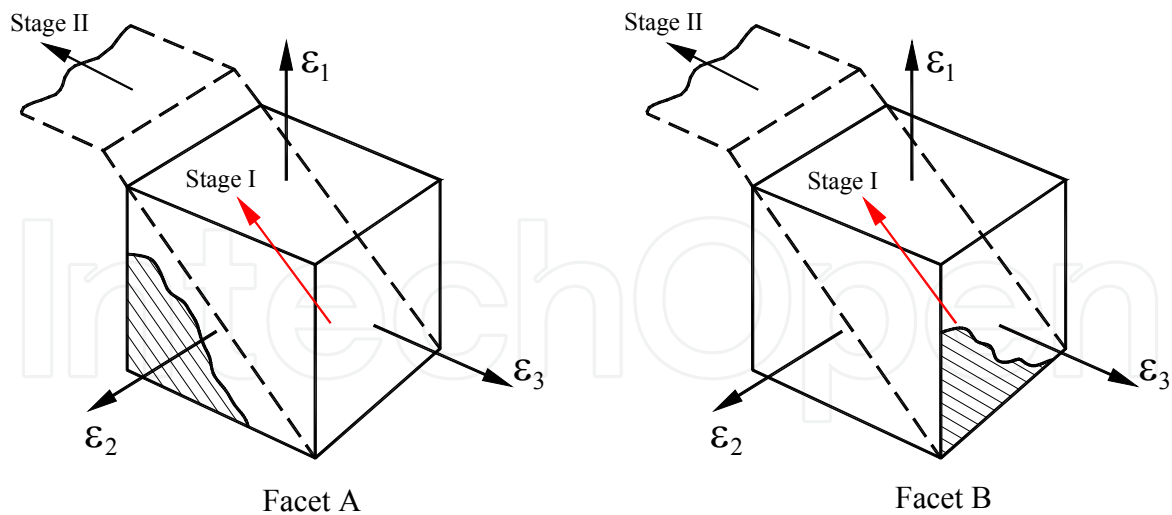
Figure 20. Directional aspect of the fatigue damage. Importance of the stress field orientation with respect to the plans surface, and the free surface of the material (hatch zones) [23, 24].

Additionally to the fatigue damage mechanism mentioned previously, in the case of welding, the stress concentration factor due to the geometry of the welding bead has a special importance. In this sense, Ambriz et al. [20] has been quantified the effect of the welding profile generated by modified indirect electric arc (MIEA) technique on the fatigue life of a 6061-T6 aluminum alloy. In order to determine the stress concentration factor K_t in MIEA welds, a characteristic welding profile was measured as specified in Figure 21.
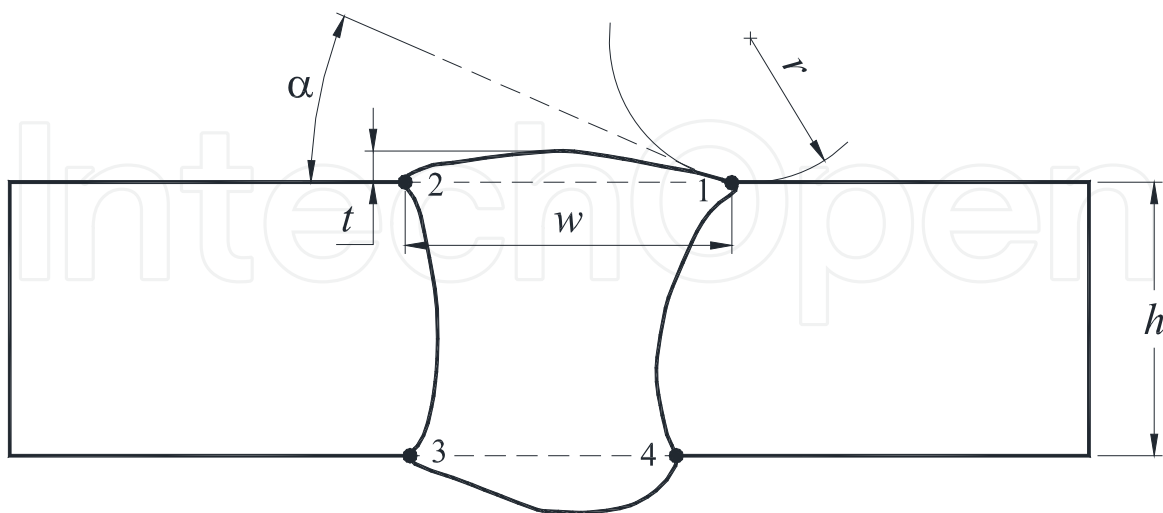

Figure 21. Stress concentration points in MIEA welds and their corresponding dimensions. α=angle formed by the weld reinforcement with plates, *r*=notched radius, *t*=height of the weld reinforcement, *w*=width of the welding profile and *h*=thickness of the plates.

Subsequently, uniaxial fatigue test a cyclic loading with a sinusoidal wave form at a frequency of 35 Hz and load ration R=0.1 was applied in atmospheric air at room temperature. The fatigue limit (77 MPa) was calculated employed the Locati method, and Wöhler curve (Figure 22) was plotted between 77 and 110 MPa.
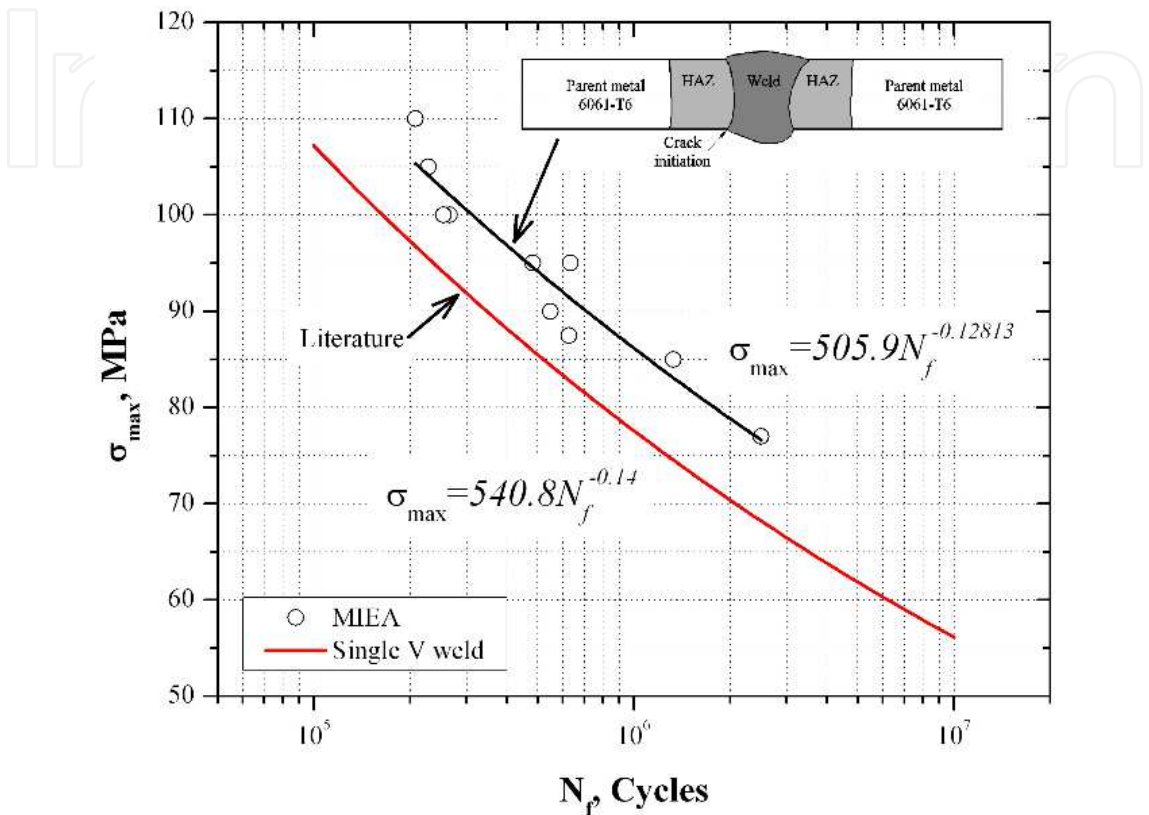

Figure 22. Wöhler curve for 6061-T6 aluminum alloy welds by MIEA and data found in literature [25] for the single V groove joint.

Figure 22 shows the maximum stress σ_{max}, as function of number of cycles to failure N_f, obtained from the fatigue test of the welded joints. The experimental results were fitted according to the following expression:

$$\sigma_{max} = AN_f^b \tag{12}$$

where A, and b are experimental values determined by fitting curve.

Regarding the geometry of the welding profile, comparison of the fatigue performance exhibited by MIEA welds with the results reported in the literature [25] for a single V joint configuration for the same aluminum alloy shows a significant improvement in fatigue life for the MIEA welded samples. The K_t effect on the crack initiation and failure is shown in Figure 23.

Figure 23. Typical macrograph of the fatigue failure on MIEA welds.

Considering that, if the loading condition promotes the formation of a principal crack (Figure 19), it will grow according to the power law region as shown schematically in Figure 24.
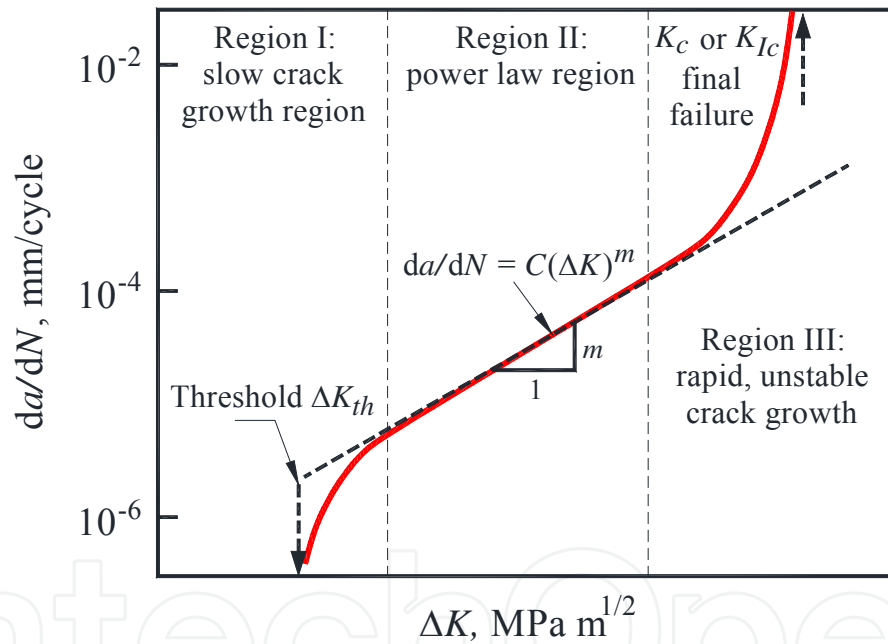

Figure 24. Fatigue crack growth regimes as function of ΔK.

The fatigue crack growth rate da/dN, as function of stress intensity factor range ΔK in different zones of the welded joint (base metal, weld metal and HAZ) has been studied previously [26, 27]. The results were conducted on compact type specimens (CT) applying a constant amplitude cycling load with a sinusoidal wave form at a frequency of 20 Hz, a load ratio R of 0.1 and a load range of 2.5 kN in atmospheric air at room temperature. The ΔK was computed by means of the following equation:

$$\Delta K = \frac{\Delta P\left(2 + \dfrac{a}{W}\right)}{BW^{1/2}\left(1 - \dfrac{a}{W}\right)^{3/2}}\left[0.886 + 4.64\frac{a}{W} - 13.32\left(\frac{a}{W}\right)^2 + 14.72\left(\frac{a}{W}\right)^3 - 5.6\left(\frac{a}{W}\right)^4\right] \qquad (13)$$

where a is the crack length of the sample (initial crack of 8 mm), W the width for the crack propagation, and B the thickness of the sample (5 mm in this case).

Considering the stable crack growth propagation region shown in Figure 24, the experimental results of a were plotted in da/dN versus ΔK graphs according to the following expression:

$$\frac{\mathrm{d}a}{\mathrm{d}N} = C(\Delta K)^m \qquad (14)$$

where C and m are constants obtained from the fitting curve. Table IV summarizes the best fitted values for C and m, and their correlation factor.

Material	C	m	R^2
6061-T6 (rolling)	5.00×10^{-7}	2.426	0.89
6061-T6 (transverse)	3.97×10^{-8}	3.320	0.97
Weld metal	2.63×10^{-14}	8.550	0.92
HAZ	3.77×10^{-9}	6.650	0.89

Table 4. Fitting constants obtained from experimental values (Figure 25) [27].

Figure 25, shows the fatigue crack growth for base metal (6061-T6) in the rolling and transverse to rolling direction.

This graph shows that the microstructural characteristics (anisotropy) does not have an important influence in terms of fatigue crack growth as could be expected, taking into account that yield strength in rolling direction is higher than transverse direction. However, this is not the case for weld metal and HAZ (Figures 25b and c), in which the crack tends to propagate faster than that in base metal. In the case of weld metal (Figure 25 b), the faster crack growth rate in comparison with base metal is related to the low toughness due to the high silicon (~ 5.5 wt. percent) content provided by the filler metal during welding. Similarly, for the HAZ it is possible to observe that the crack growth is faster than base metal, aspect which is attribute to the microstructural transformation of fine needle shape precipitates β″ into coarse bar shape precipitates β′ produced by the thermal effect.
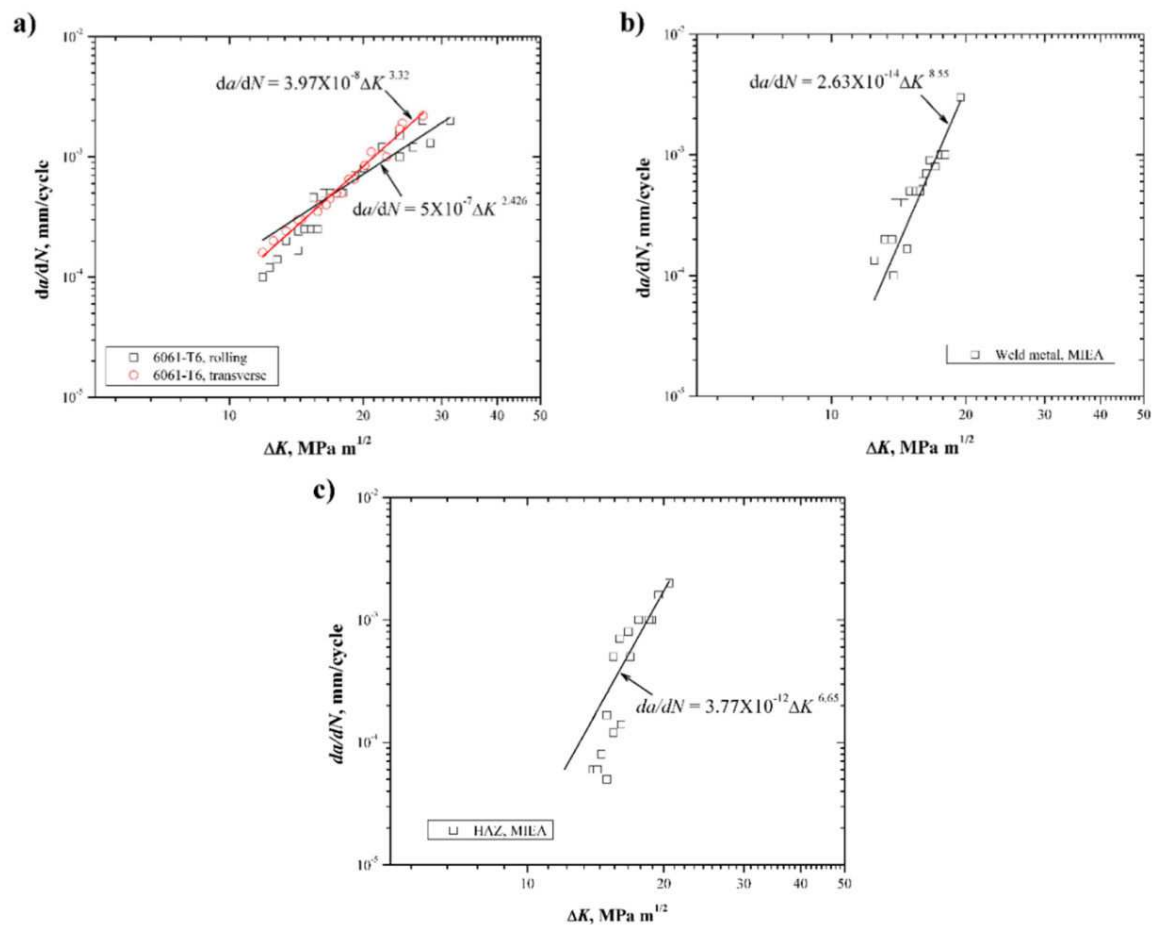
Figure 25. Fatigue crack growth rate as function of ΔK, a) 6061-T6 base metal, b) weld metal, and c) HAZ.

3. Conclusion

Mechanical behavior in welds of precipitation hardened aluminum alloys are still under development and the softening phenomena in the heat affected zone should be better understood. Valuable information could be obtained by the precise understanding of the weld thermal cycles in conjunction with the C transformation curve and its microstructural effect in mechanical properties. In this sense, our research group is conducting experiments to control the weld thermal cycle by means of localized chillers and heaters in the fusion zone and heat affected zone to observe the mechanical properties evolution of the welded joints.

Author details

R.R. Ambriz and D. Jaramillo

Instituto Politécnico Nacional CIITEC-IPN, Cerrada de Cecati S/N Col. Sta. Catarina, Azcapotzalco, DF, México

References

[1]   Gladman T. Precipitation Hardening in Metals. Materials Science and Technology 1999;15 30-36.

[2]   Orowan E. Internal Stress in Metals and Alloys; 1948.

[3]   Ashby MF. Oxide Dispersion Strengthening. Gordon and Breach; 1958.

[4]   Gladman T. The Physical Metallurgy of Microalloyed Steels. The Institute of Materials; 1997.

[5]   ASM. Properties and Selection: Non Ferrous Alloys and Special Purpose Materials. ASM International; 1992.

[6]   Askeland D., Fulay P and Wright W. The Science and Engineering of Materials; 2010.

[7]   Edwards G., Stiller K., Dunlop GL. and Couper MJ. The precipitation sequence in Al-Mg-Si alloys. Acta Materialia 1998;46 (11) 3893-3904.

[8]   Ambriz RR., Barrera G., García R. and López VH. Effect of the Weld Thermal Cycles of the Modified Indirect Electric Arc on the Mechanical Properties of the AA6061-T6 Alloy. Welding International 2010;24 (4) 42-51.

[9]   Myhr OR., Grong O., Fjaer HG. and Marioara CD. Modelling of the Microstructure and Strenght Evolution in Al-Mg-Si Alloys During Multistage Thermal Processing. Acta Materialia 2004;52 4997-5008.

[10] Matters G. The Welding of Aluminum and its Alloys. CRC; 2002.

[11] Grong O. Metallurgical Modelling of Welding. The Institute of Materials; 1997.

[12] Metzger GE. Some Mechanical Properties of Welds in 6061 Aluminum Alloy Sheet. Welding Journal 1967;46 (10) 457-469.

[13] Huang C. and Kou S. Liquation Cracking in Full Penetration Al-Mg-Si Welds. Welding Journal 2004;4 111-122.

[14] Oliver WC. and Pharr GM. An Improved Technique for Determining Hardness and Elastic Modulus Using Load and Displacement Sensing Indentation Experiments. Journal of Materials Research 1992;7 (6) 1564-1583.

[15] Malin V. Study of Metallurgical Phenomena in the HAZ of 6061-T6 Aluminum Welded Joints. Welding Journal 1995;9 305-318.

[16] Liu G., Murr LE., Niou CS., McClure JC. and Vega FR. Microstructural Aspects of the Friction Stir Welding of 6061-T6 Aluminum. Scripta Materialia 1997;37 (3) 355-361.

[17] Hay JC., Bolshakov A. and Pharr GM. Critical Examination of the Fundamental Relations Used in the Analysis of Nano-Indentation Data. Journal of Materials Research 1999;14 (6) 2296-2305.

[18] Ambriz RR., Chicot D., Benseddiq N., Mesmacque G. and de la Torre SD. Local Mechanical Properties of the 6061-T6 Aluminum Weld Using Micro-Traction and Instrumented Indentation. European Journal of Mechanics A/Solids 2011;30 307-315.

[19] Chicot D., Roudet F., Zaoui A., Louis G. and Lepingle V. Influence of Visco-Elastic-Plastic Properties of Magnetite on the Elastic Modulus: Multicyclic Indentation and Theoretical Studies. Materials Chemistry and Physics 2010;119 75-81.

[20] Ambriz RR., Mesmacque G., Ruiz A., Amrouche A. and López VH. Effect of the Welding Profile Generated by the Modified Indirect Electric Arc Technique on the Fatigue Behavior of 6061-T6 Aluminum Alloy. Materials Science and Engineering A 2010;527 2057-2064.

[21] Pineau A. and Bathias C. Fatigue des Matériaux et des Structures 1. Lavoisier; 2008.

[22] Forsyth PJE. Some Metallographic Observations on the Fatigue of Metals. Journal of the Institute of Metals 1951;80 181.

[23] Brown MW. and Miller KJ. A Theory for Fatigue Failure Under Multiaxial Stress-Strain Conditions. Proceedings of the Institution of Mechanical Engineerings 1973;187 745-755.

[24] Miller KJ. Metal Fatigue-Past, Current and Future. Proceedings of the Institution of Mechanical Engineerings 1991;205 1-14.

[25] ASM. Fatigue and Fracture. ASM Iternational; 1996.

[26] Moreira PMGP., de Jesus AMP., Ribeiro AS. and de Castro PMST. Fatigue Crack Growth in Friction Stir Welds of 6082-T6 and 6061-T6 Aluminium Alloys: A Comparison. Theoretical and Applied Fracture Mechanics 2008;50 81-91.

[27] Ambriz RR., Mesmacque G., Ruiz A., Amrouche A., López VH. and Benseddiq N. Fatigue Crack Growth Under a Constant Amplitud Loading of Al-6061-T6 Welds Obtained by Modified Indirect Electric Arc Technique. Science and Technology of Welding and Joining 2010;15 (6) 514-521.